November 9, 2021 Volume 37, Number 44 pubs.acs.org/Langmuir

LANGMUIR

The ACS journal of fundamental interface science

ACS Publications
Most Trusted. Most Cited. Most Read.

www.acs.org

LANGMUIR

pubs.acs.org/Langmuir Article

Mesoporous TiO_2 Microparticles with Tailored Surfaces, Pores, Walls, and Particle Dimensions Using Persistent Micelle Templates

Wessel van den Bergh, Eric R. Williams, Natalie Alicia Vest, Pei-Hua Chiang, and Morgan Stefik*

Cite This: *Langmuir* 2021, 37, 12874–12886 Read Online

ABSTRACT: Mesoporous microparticles are an attractive platform to deploy high-surface-area nanomaterials in a convenient particulate form that is broadly compatible with diverse device manufacturing methods. The applications for mesoporous microparticles are numerous, spanning the gamut from drug delivery to catalysis and energy storage. For most applications, the performance of the resulting materials depends upon the architectural dimensions including the mesopore size, wall thickness, and microparticle size, yet a synthetic method to control all these parameters has remained elusive. Furthermore, some mesoporous microparticle reports noted a surface skin layer which has not been tuned before despite the important effect of such a skin layer upon transport/encapsulation. In the present study, material precursors and block polymer micelles are combined to yield mesoporous materials in a microparticle format due to phase separation from a homopolymer matrix. The skin layer thickness was kinetically controlled where a layer integration via diffusion (LID) model explains its production and dissipation. Furthermore, the independent tuning of pore size and wall thickness for mesoporous microparticles is shown for the first time using persistent micelle templates (PMT). Last, the kinetic effects of numerous processing parameters upon the microparticle size are shown.

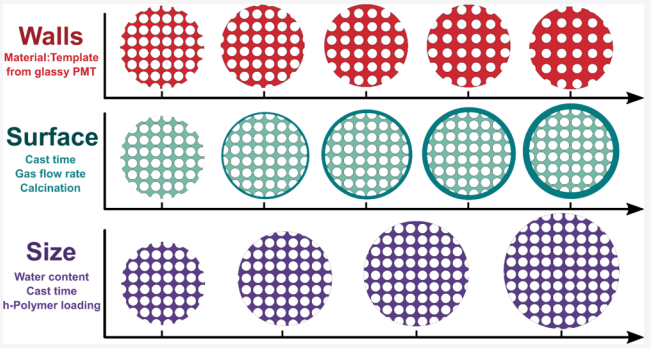

INTRODUCTION

Mesoporous microparticles enable convenient integration of nanomaterials with popular manufacturing methods based on micron-scale powders. Applications of mesoporous microparticles include drug delivery,[1−5] chemical sensors,[6−9] catalytic structures,[10−22] and energy devices.[23−43] The application performance depends upon the architecture of the nanostructure where the transport and storage of drugs or intercalation of ions are influenced by the pathways and interfaces. The presence of a less-porous skin layer can further tailor chemical transport rates to/from the microparticle, for example, adjusting the rate of controlled release.[1−3,13,44,45] Thus, the ability to custom tailor each aspect of the mesoporous microparticle architecture determines the ultimate performance. For example, when mesoporous microparticles are applied in battery electrodes, each architectural dimension contributes toward a specific function: the wall thickness determines the ion intercalation length scale, the particle size and porosity determine the electrolyte diffusion length, and the surface area influences the insertion kinetics. Efficient electrode design balances these concomitant processes to achieve the greatest gravimetric and volumetric energy/power densities.[46] Such tailored mesoporous microparticles could also provide a platform for investigating emergent nanoscale phenomena using fully tailorable nanomaterials to deconvolve contributions from concomitant processes.[47] Synthetic routes for both soft and hard templates have widely enabled mesoporous microparticles.[4,5,9,14−18,25−29,48−65] Soft templates are advantageous in terms of the lower cost, simpler preparation, and synthetic versatility. Soft template routes span a wide gamut, including hydro/solvothermal synthesis,[14,19−21,30−35,43,48,49,66−70] spray pyrolysis,[5,18,25,27,52−61,63,65] and evaporative casting.[9,15−17,26,28,29,50,51,71] Generally, the microparticle structure is controlled via the dispersion of precursors. For example, spray pyrolysis techniques quickly form microparticles from the evaporation of aerosols; however, the nanostructures are often poorly defined and the microparticles are sometimes covered with a skin layer with a speculative formation pathway.[53,54,56−58,63,64] Hydro/solvothermal synthesis techniques and simple evaporative casting processes produce microparticles via phase separation of precursors from a solvent or a non-volatile species such as a homopolymer. These approaches have demonstrated many different morphologies and numerous different nanoscale

Received: July 13, 2021
Revised: September 13, 2021
Published: October 7, 2021

https://doi.org/10.1021/acs.langmuir.1c01865
Langmuir 2021, 37, 12874−12886

dimensions via soft templates; however, none have yet demonstrated independent control of the pore and wall dimensions. This lack of one variable at a time tailoring is in part due to the changing of micelle template dimensions with alterations to processing conditions. A fully tunable strategy must be able to adjust all feature sizes in a controlled and predictable manner.

Persistent micelle templates (PMTs) uniquely enable nanostructures with independent tunability of the pore and wall dimensions.[47,72−76] Most processes using block polymer structure-directing agents are based upon equilibration, and thus, the architectural dimensions are determined by free-energy minimization. In contrast, the PMT strategy is based upon kinetic control where block polymer micelles are used as templates with an invariant size. Here, it is important to inhibit chain-exchange processes which would otherwise cause the micelles to change their size in response to changing solution conditions. The equilibrium size of a micelle is a balance of enthalpic and entropic contributions, largely tied to interfacial energy (favoring larger micelles) and chain stretching entropy (favoring smaller micelles). The activation energy for chain exchange naturally determines its rate. For the single chain-exchange mechanism, the rate has a double-exponential dependence on χN, where N scales with core block molecular mass and χ is the Flory−Huggins interaction parameter, a largely enthalpic term corresponding to the two-component interface of the core block with the solution ($\chi_{\text{core-solution}}$).[77,78] The use of such high-χN conditions was shown to enable the kinetic entrapment of persistent micelles to yield constant template dimensions.[73] The material wall thickness may be tailored monotonically by changing the amount of material precursors relative to the amount of template (M:T ratio) and the resulting feature sizes follow a simple geometric model.[72] PMT thus diverges from dynamic (non-persistent) micelle templates which undergo size changes due to equilibration anytime the M:T ratio is altered, which leads to chaotic trends of the feature sizes[72] as well as changes to the morphology.[79] In the past, PMT approaches were mostly used for thin films where the rapid material cross-linking ensured preservation of kinetic micelle control after evaporation.[47,72−75]

The development of fully tunable bulk mesoporous microparticles with PMT thus poses several design challenges. Here, an evaporative strategy is adopted based upon micelle templates, material precursors, and a phase-separating homopolymer. The evaporative processing of microparticles from the bulk solution is inherently slower than thin-film spin coating and thus provides numerous challenges toward preserving kinetic control of micelle templates. Both the removal of solvents that inhibit chain exchange (particularly water) and the subsequent heat treatments to cross-link the material precursors enable additional time for a loss of kinetic control via equilibration. Here, it is shown that simple translation of prior PMT protocols toward mesoporous microparticles resulted in a loss of kinetic micelle control. This lack of independent pore and wall thickness control is a general feature of other evaporative casting works. An improved PMT strategy was developed to yield the first mesoporous microparticles prepared from block polymers that independently control the pore and wall thickness based upon micelles with glassy cores (glassy-PMT).[76] This use of micelles with robust kinetic entrapment was necessary to preserve the micelle shape and size throughout the full synthesis. This contrasts with prior evaporative casting works which were subject to multiparameter changes when glassy templates were plasticized[9,26] or when low-T_g templates were used.[14−17,28,29,50,51,71] While there are a broad range of mesoporous carbon,[22,23,30,37,66,76,80] metal,[55,81−83] oxide,[1−5,7−13,20,21,24,25,31,34,35,40−42,44,45,47,51−54,57−62,64,67,70,72,73,79,84,85] hydroxide,[65,71] sulfide,[32,69] and polyanion[10,43] materials reported, TiO_2 was selected here as a model material due to its broad use in catalysis,[14−19,48,50,56,63] energy storage,[26,68,74] sensing,[38,86] and other applications.[27−29,33,36,49] Furthermore, processing factors that determine skin layer thickness and particle size were identified. A model is presented to explain skin layer formation and is used to tailor the microparticle surface. Thus, a comprehensive set of conditions are elaborated to enable custom tuning of all architectural aspects of mesoporous microparticles.

EXPERIMENTAL SECTION

Materials. Methanol (MeOH, 99.8%, Fisher) and ethanol (EtOH, 200 proof, ACS Grade, Fisher) were dried at room temperature (RT) by storage over 30% w/v of molecular sieves (3 Å, 8−12 mesh, Acros Organics) for a week.[87] *n*-Butyl acrylate (≥99%, Acros Organics) and the styrene (99%, Acros Organics) monomer were passed through a basic alumina column just prior to use. Poly(propylene glycol) (PPO, M_n = 1000 and 4000 g mol^{-1}, Sigma-Aldrich) was placed under vacuum overnight at RT before use to remove residual water. 2-Bromopropionic acid (>99%, Aldrich), 4-(dimethylamino) pyridine (99%, Aldrich), aluminum oxide (Al_2O_3, basic, Brockmann I, 50−200 μm, Acros Organics), chloroform (>99%, Aldrich), copper(I) bromide (99.99%, Aldrich), dimethylformamide (97%, Aldrich), hexanes (>98.5%, Fisher), concentrated hydrochloric acid (HCl, 37% w/w, ACS grade, VWR), anhydrous magnesium sulfate ($MgSO_4$, 99%, J.T. Baker), poly(ethylene glycol) methyl ether (PEO-OH, M_n = 5000 g mol^{-1}, Aldrich), tetrahydrofuran (THF, ACS Grade ≥99.0%, Fisher), titanium(IV) isopropoxide (TTIP, ≥98%, Acros Organics), and tris-(2-dimethylaminoethyl) amine (97%, Aldrich) were used as received.

Polymer Synthesis and Characterization. Poly(ethylene oxide-*b*-butyl acrylate), PEO-*b*-PBA, and poly(ethylene oxide-*b*-styrene), PEO-*b*-PS, diblock polymers were synthesized by a two-step synthesis. First, a Steglich esterification of poly(ethylene glycol)methyl ether was used to form a macroinitiator for atom-transfer radical polymerization (ATRP). Second, ATRP was used to grow the PBA or PS block from the macroinitiator. The procedure is described elsewhere in detail (Supporting Information, Table S1).[72] The molar mass of PBA or PS blocked was determined using a Bruker Avance III HD 300 ^{1}H NMR by comparison to the known PEO block molecular weight (Supporting Information, Figures S1a and S2a and Table S2). ^{1}H NMR of PEO-*b*-PBA (300 MHz, $CDCl_3$) δ (ppm): 4.05 ($COOCH_2$), 3.67 ($O-CH_2CH_2-O$), 2.30 ($CHCOO$), 1.92 ($-CH_2CH-$), convolved peaks 1.62 ($-CH_2-$, $-CH_3$), 1.39 ($-CH_2-$, $-CH_3$) and 0.96 ($-CH_2-$, $-CH_3$) with some contribution from 1.92 ($-CH_2CH-$). ^{1}H NMR of PEO-*b*-PS (300 MHz, $CDCl_3$) δ (ppm): convolved peaks 7.09 (o,p,m C−H) and 6.56 (o,p,m C−H), 3.67 ($O-CH_2CH_2-O$), convolved peaks 1.86 ($-CH_2CH-$, $-CH_2CH-$) and 1.45 ($-CH_2CH-$, $-CH_2CH-$). The molar mass dispersity index was characterized using a Waters gel permeation chromatography (GPC) system equipped with a Waters 1525 binary pump, three styragel columns (HR1, HR3, and HR5 in the effective molecular weight ranges of 0.1−5, 0.5−30, and 2−400 kg mol^{-1}, respectively), and a Waters 2414 refractive index detector (Supporting Information, Figures S1b and S2b and Table S2). The GPC system was calibrated with poly(styrene) standards (1.50, 3.28, 10.00, 17.40, 32.70, 120.00, 214.00, 545.00, and 1010.00 kg mol^{-1}) obtained from Polymer Standards Service GmbH. GPC samples were prepared in THF at a concentration of 5 mg mL^{-1} and were passed through a 0.2 μm syringe filter prior to injection. Note that the monochelic PEO-OH had a bimodal GPC trace as-received from the manufacturer

https://doi.org/10.1021/acs.langmuir.1c01865
Langmuir 2021, 37, 12874−12886

(Supporting Information, Figures S1b and S2b), a contaminant feature that was also apparent after further polymerization and was included in molar mass dispersity ($Đ$) calculations (Supporting Information, Figures S1b and S2b).

Micelle Template Preparation. The PEO-*b*-PBA micelle stock solution was prepared by dispersing 40 mg of PEO-*b*-PBA in 4 mL of MeOH at RT with gentle agitation. Concentrated HCl was added slowly to achieve the target water composition of 0.7 wt % similar to prior work,[74] with respect to the total mixture unless otherwise stated (examined 0.7−20%). The combined solution was sonicated using a Fisher ultrasonic bath (Cat. no. FS-28) operated continuously at full power (225 W) and a frequency of 40 kHz for 10 min at RT, intended to temporarily enable chain exchange.[85,88] The micelle stock was then divided into aliquots containing 8 mg of the polymer template in preparation of each M:T evaporative casting condition.

The PEO-*b*-PS micelles were prepared by dissolving 1.0 g of PEO-*b*-PS in 10 mL of THF in a large round-bottom flask.[76] To this solution was added 10 mL of deionized water in a dropwise fashion and with frequent swirling of the flask. Next, 100 mL of anhydrous methanol was added. THF was removed by rotary evaporation, and the removed volume was replaced with anhydrous methanol to achieve a final micelle concentration of 10 mg mL^{-1}. It was previously shown that a procedure such as this is important to remove all good solvents which act as plasticizers.[76] Subsequently, anhydrous $MgSO_4$ was added in excess to the solution until a cloudy precipitate was observed, indicating a preliminary state of dryness. The mixture was passed through a Gelman Sciences glass fiber filter paper with 1 μm pores to remove this precipitate and yield a transparent solution with a much lower water content. This solution was then further dried over molecular sieves (3 Å, 8−12 mesh) and allowed to sit for at least 3 days before use. Similar drying conditions were shown to lead to <40 ppm levels of water.[87] Just prior to use, concentrated HCl was added slowly to 4 mL of the micelle solution to reach a desired water composition, 10 wt % with respect to the total stock solution unless otherwise stated. The resulting micelle stock solution was divided into aliquots containing 8 mg of the polymer template for the preparation of each M:T evaporative casting condition.

***Ex Situ* Sol Method.** An *ex situ* TiO_2 sol stock was used as described in detail elsewhere.[74] Briefly, 5 mL of titanium isopropoxide (TTIP) was added to 1.2 mL of rapidly stirring concentrated HCl (37% wt %), creating a solution with a 3:1 H_2O/Ti ratio. Note that this reaction is very exothermic. After being allowed to cool for a few minutes, 2 mL of anhydrous MeOH was added to dilute the sol stock solution. This dilute sol stock solution was combined with one of the micelle template stock solutions described above in varying ratios, depending on the target material to template (M:T) ratio. Here, the M:T ratio is calculated by comparing the anticipated final oxide mass (e.g., TiO_2) relative to the mass of the block polymer template.

Mesoporous Microparticle Synthesis. In a typical experiment, the micelle stock solution was combined with the dilute *ex situ* sol stock solution, followed by the addition of the prescribed amount of 1.0 kg mol^{-1} poly(propylene oxide). The PPO loading was reported as a mass ratio relative to the block polymer template. The PPO loading was 10× (examined 2.5×−40×) unless otherwise stated. Unless stated otherwise, the solution was bulk-cast within a 9.0 cm glass dish and tilted around to assure uniform wetting of the dish. Unless otherwise noted, a glass cover was placed on the dish with a spacer made from 16G copper wire (see Supporting Information, Figure S3). The covered dish was then placed in a Tupperware chamber with a constant flow of air. Unless otherwise noted, the purge gas was 16 L/min (examined 0.1−25 L/min) with 15% relative humidity as controlled using a homemade system.[73] Unless otherwise noted, the dish was left to dry for 3 h and was then directly transferred to the "aging" process to promote cross-linking of material precursors. Samples were aged by placing them in a vacuum oven at RT and slowly reducing the pressure over 30 min to avoid damage to the nanostructure. The aging treatment was customized for each polymer template. For PEO-*b*-PBA templates, the samples were held for 12 h of RT vacuum and were then further heated to 190 °C for 12 h (examined 40−190 °C). For PEO-*b*-PS templates, the samples were heated in the vacuum oven to 80 °C overnight. In both cases, the resulting aged samples were then calcined at 450 °C for 0.1 h with a 5 °C min^{-1} ramp, unless otherwise stated, to oxidatively remove the polymer and induce crystallization of the material. Please note that the removal of the homopolymer or block polymer template by dissolution has been shown elsewhere as an alternative to removal via calcination.[82,83,89−92]

Small-Angle X-ray Scattering Measurements. X-ray experiments were conducted using a SAXSLab Ganesha at the South Carolina SAXS Collaborative (SCSC). A Xenocs GeniX 3D microfocus source was used with a copper target to produce a monochromatic beam with a 0.154 nm wavelength. The instrument was calibrated prior to measurements using the National Institute of Standards and Technology (NIST) silicon reference material, 640 d with the peak position at 2θ = 28.44°. A Pilatus 300k detector (Dectris) was used to obtain the 2D scattering patterns with nominal pixel dimensions of 172 × 172 μm. Transmission small-angle X-ray scattering (SAXS) data were measured. SAXS data were obtained with an X-ray flux of ∼3.3 M photons per second upon the sample and a detector-to-sample distance of 1040 mm. The 2D images were azimuthally integrated to yield the scattering vector and intensity. Peak positions were fitted using custom MATLAB software. Transmission wide-angle X-ray scattering (WAXS) data were measured to identify the crystalline phase of mesoporous microparticles and were obtained with an X-ray flux of ∼36 M photons per second upon the sample and a detector-to-sample distance of 112 mm. The 2D images were azimuthally integrated to yield the scattering vector and intensity. A Gaussian point-spread function was utilized to interpret scattering data as a result of grain-size broadening as per the Scherrer formula.[93,94]

Scanning Electron Microscopy Measurements. Top-view images of calcined particles were obtained with a Zeiss Ultraplus thermal field emission scanning electron microscopy (SEM) system using an accelerating voltage of 5 keV and an in-lens secondary electron detector, and the working distance was maintained at ∼2.5 mm. The skin layer thickness was measured using cross-section images of fractured microparticles. For samples containing significant fractions of open and accessible porosity (no skin layer), the measured skin layer thicknesses were weighted by the area fraction of skin layer coverage. Pore and wall size measurements were carried out exclusively on images measured at 200K× magnification to eliminate calibration variation during SEM measurements. The wall thickness was measured by inscribing the largest possible circle between pores and recording the corresponding diameter.[74] The particle size distributions were determined manually by measuring 150 particles within a randomly selected image section for each condition. The full histograms are presented along with the mean, error of the mean, and standard deviation. Measurements of skin layer thickness, area fraction of open surface porosity, pore, wall, and particle size were all determined using ImageJ software.

RESULTS AND DISCUSSION

Ideally, the synthesis of mesoporous microparticles supports independent tailoring of each feature size, including skin layer thickness or absence thereof, pore size, wall thickness, and microparticle size. Prior works have demonstrated the ability to adjust several of these dimensions, although generally coupled at the same time with changes to other feature sizes.[16,26,28,48,57,66,80] The independent adjustment of the pore size, wall thickness, or skin layer thickness has remained elusive for mesoporous microparticles produced using soft templates. Here, we employ a polymer-based soft template strategy to produce mesoporous microparticles by combining a block polymer with a phase-separating homopolymer. Through evaporative processing with a common solvent, the block polymer and material precursors phase-separate from the homopolymer. Several important design criteria must be considered to realize mesoporous microparticles with

https://doi.org/10.1021/acs.langmuir.1c01865
Langmuir 2021, 37, 12874−12886

independent feature tunability in this context. (1) The mixture of polymers must use a majority of the homopolymer such that the other components (a mixture of the block polymer and material precursors) phase-separate as a minority suspension of discrete microparticles. Most prior examples employ a 5−10× ratio of the homopolymer to other reagents to inhibit coarsening of the minority phase by avoiding percolation and extending the distance between the microparticles. (2) The homopolymer composition must be selected to phase-separate from both the block polymer ($\chi_{\text{homopolymer-template}} > 0.5$) and material precursors ($\chi_{\text{homopolymer-precursor}} > 0.5$). Selecting a homopolymer with a different chemical composition from the block polymer generally will lead to the desired phase separation; otherwise, the homopolymer may swell the block polymer phase.[84] Furthermore, popular material precursors, for example, metal oxide nanoparticles, are hydrophilic due to hydrogen bonding interactions and have limited solvent options. Thus, the homopolymer must be processable from common hydrophilic solvents yet be sufficiently hydrophobic to phase-separate from the material precursors. The homopolymer poly(propylene oxide) satisfies all these considerations. (3) The block polymer within the microparticle minority phase must also satisfy several concomitant criteria. A portion of the block polymer must phase-separate from the material precursors ($\chi_{\text{core-precursor}} > 0.5$) to produce a nanostructure, eventually leading to mesoporosity after thermal removal of the polymers. Furthermore, the other portion of the block polymer must selectively interact with the material precursors ($\chi_{\text{corona-precursor}} < 0$), typically via hydrogen bonding. Last, the block polymer must also be dispersible in the same solvent used for the other components, often lower alcohols. PEO-*b*-PBA satisfies all these criteria and PEO-*b*-PS can also satisfy these criteria when pre-micellized, *vide infra*. (4) Considering that multiple materials undergo simultaneous phase separation and rearrangement, the timescale of evaporation should be controlled to tailor the spatial distribution of each component (Scheme 1). It will be shown that deliberate rate control during evaporation enables regulation of the skin layer thickness and particle size. (5) Retaining independent control of the pore and wall dimensions requires that the block polymer template does not undergo equilibration.[72−75,84] In contrast, a kinetically trapped process called PMT enables independent and precise control of these dimensions with as small as 2 Å increments of adjustment demonstrated between samples.[72,74] Most prior PMT demonstrations produced thin films and relied upon arresting chain exchange between micelles by imposing a large $\chi_{\text{core-solution}}$.[73,75] In contrast to past works involving ∼100 to 500 nm thin films which can evaporate the solvent and cross-link the oxide within seconds, it is shown here that the novel use of glassy micelle cores was needed to impose persistence on the more extended timescales needed for bulk samples.

Skin Layer Control. Surface skin layers regulate the transport of reagents to and from microparticles. Skin layers around mesoporous microparticles have been observed elsewhere; however, their presence is rarely explained and is sometimes attributed to rapid evaporation of the solvent[53,54,57,59] or thermodynamics.[95] While some adjustment of the skin layer has been reported, these syntheses did not independently modify other structural features.[57,63,95] The preliminary experiments leading to this report often resulted in microparticles with a significant skin layer thickness (Figure 1c). The skin layer formation was examined under different processing times as well as different evaporation conditions (purge 0.1−25 L/min). Here, the term "processing time" indicates the time from the beginning of solution evaporation until the sample was transferred from the drying chamber to the aging step which promotes material cross-linking. The samples dried with 25 L/min of the carrier gas exhibited a marked reduction in the skin layer thickness upon extension of this processing time. Please note that most of the solvent has left the sample within the first 5 min, whereas the skin layer was found to monotonically reduce in thickness for 3 h, exhibiting a final average thickness of 14.2 ± 2.4 nm. The

Scheme 1. Casting Solution with Homogeneous Dispersion of Homopolymers (Green), Block Polymer Micelles (Red and Blue), Material Nanoparticles (Black), and Solvent Molecules (Not Drawn) (a); Evaporation of the Solvent Leads to Phase Separation of the Nanoparticles and the Micelles from the Homopolymer; Here, Different Rates of Phase Separation for the Nanoparticles and the Micelles Lead to the Formation of a Skin Layer on the Exterior of the Microparticles (b); Over Time, the Sol Particles Redistribute throughout the Corona Blocks of the Micelles, Reducing the Skin Layer Thickness (c); Such a Process Would Release Free Energy by Minimizing Nanoparticle Contact with the Homopolymer and Maximizing Nanoparticle Contact with the Corona Blocks. Similarly, Some Nanoparticles Could Phase-Separate away from the Micelle Templates

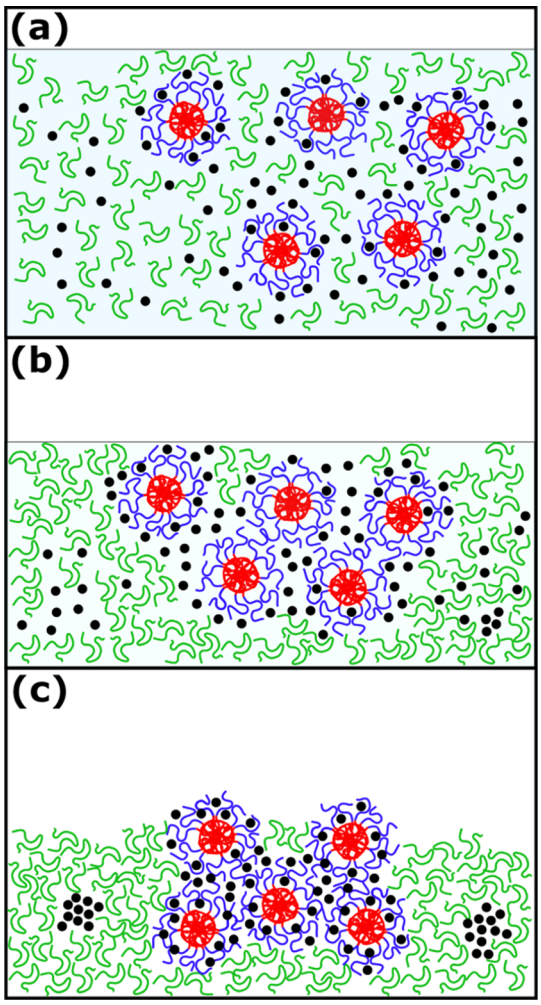

https://doi.org/10.1021/acs.langmuir.1c01865
Langmuir 2021, 37, 12874−12886

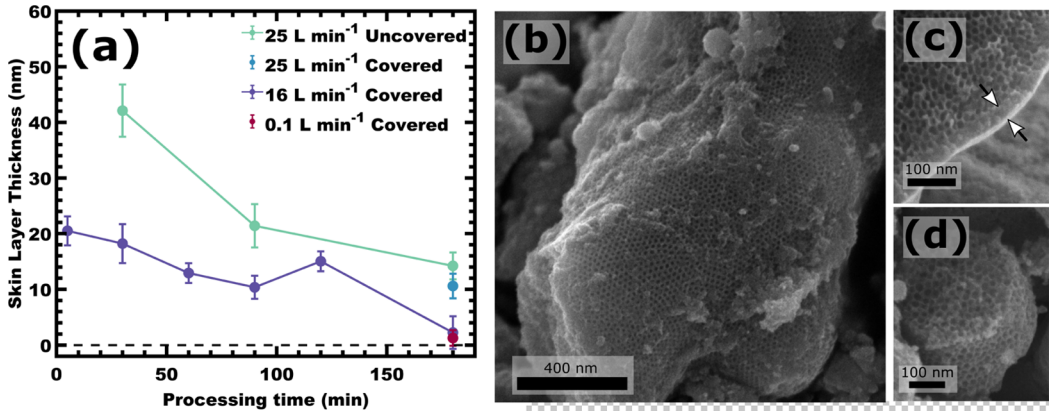

Figure 1. Skin layer thickness at the surface of mesoporous microparticles was varied with different processing parameters (a). SEM image of a representative microparticle without a skin layer (b) reveals accessible porosity. Cross-sectional SEM images of fractured microparticles were used to determine skin thickness statistics (c,d). Values are reported as the mean ± error of the mean. Data and SEM images shown for PEO-*b*-PBA with M:T = 2.5.

pronounced trend for processing time dependence indicates kinetic control. Furthermore, partially covering the dishes and/or reducing the gas flow rate to 16 or 0.1 L/min were all found to reduce the skin layer thickness (Figure 1a). The thinnest skin layer thickness of 1.28 ± 1.40 nm (with 71% of open porosity) was found using 0.1 L/min of the carrier gas with a partially covered dish (Supporting Information, Figure S3). Longer processing times generally lead to thinner skin layers and greater degrees of open surface porosity (no skin layer) across all conditions, except for the 120 min sample under 16 L/min. Samples dried under 16 L/min of the carrier gas reached a minimal skin layer thickness of 2.25 ± 2.93 nm with 86% open porosity. Both the 16 and 0.1 L/min flow rate conditions with a sufficient processing time of 3 h or more produced microparticles with a majority of open mesoporosity (Figure 1b,d). The use of tailored drying gas flow rates has not been previously examined for block polymer-based mesoporous microparticles. We propose that the skin layer formation is caused by different rates of phase separation for each of the microsphere components: the block polymer micelles and the material precursors. As the solvent is gradually eliminated, the initially homogeneous solution (Scheme 1a) begins to partition and phase-separate during drying (Scheme 1b) as governed by the solubility and mobility of each component. These differences can lead to an uneven distribution of material precursors and block polymer micelles. Consider the process where a nanoparticle (material precursor) is added to a cluster of micelles composing a microsphere; the nanoparticle incorporation into the surface is reasonably much faster than its diffusion into the micelle corona chains. Given enough time and mobility, the nanoparticles accumulating at the surface of the microparticles can be integrated within the microspheres (Scheme 1c). While full incorporation is expected considering nanoparticle diffusion rates in polymer melts,[96−99] the inability of our samples to reach that state suggests that the nanoparticle cross-linking rate competes with the nanoparticle incorporation rate to generally preserve some skin layer. Regardless, we term this process layer integration via diffusion (LID). The LID model explains why skin layers are found most commonly for spray pyrolysis methods[53,54,56−60,64,65] which have rapid evaporation but slower methods often do not exhibit a skin layer.[16,26,28,50,51] Similarly, the process examined here spans in behavior from a tunable skin layer to mostly eliminating the skin layer. Other recent studies have demonstrated that the interfacial energetics can impose/eliminate a skin layer, albeit coupled with variation of multiple architectural parameters at the same time.[80] The skin layer is also adjustable at later steps via thermal coarsening. Figure 2 shows how progressively

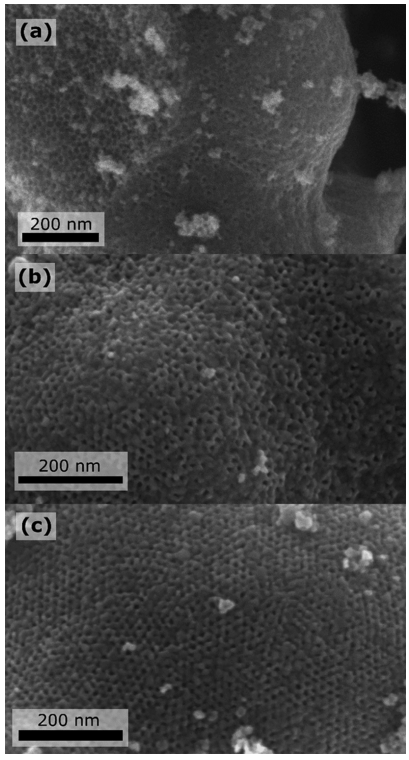

Figure 2. SEM images of microparticle surfaces showing the pore exposure, or lack thereof, for the same starting sample tailored via different subsequent calcination conditions: 0.1 h (a), 12 h (b), and 24 h (c) at 450 °C. The template was PEO-*b*-PBA with M:T = 2.5.

increasing the calcination time leads to the gradual reduction of the surface layer, likely driven by the reduction of surface area. Please note that SAXS measurements on these thermally coarsened nanostructures revealed no marked changes to the well-defined nanostructure (Supporting Information, Figure S4). Thus, the LID model and thermal coarsening enable

https://doi.org/10.1021/acs.langmuir.1c01865
Langmuir 2021, 37, 12874−12886

tailoring of the skin layer thickness via kinetic control and can include a majority of open surface mesoporosity.

Independent Pore and Wall Control via PMTs. The mesopore size and wall thickness are important to control since they govern intraparticle species transport through the nanostructure and intercalation transport into the nanostructure, respectively, thus significantly influencing application performance. As introduced earlier, PMT enables the independent tuning of nanoscale pore and wall dimensions by using kinetically trapped micelle templates. As quantitatively predicated by a prior SAXS-based model, a PMT series is expected to exhibit lattice expansion when the template size is held constant and the material is added between micelles (increasing M:T ratio).[72] Such lattice expansion is simple to validate quantitatively via the primary SAXS peak shifting to lower q (higher d-spacing). However, the PEO-*b*-PBA-based samples did not exhibit such a trend in SAXS peak position shift (q-spacing) and was rather indicative of lattice contraction typical for dynamic micelle (not PMT) behavior (Figure 3a). Furthermore, the SAXS patterns were often bimodal, indicative of multiple morphologies and partial equilibration.[54,62] These results suggest that after evaporation, the material precursors surrounding the micelles are insufficient to hamper chain exchange, neither in terms of energetic barrier (χN) nor mobility hindrance from, for example, condensation reactions. This shows that the preservation of kinetic control is more challenging here than with prior thin-film methods. Most prior PMT demonstrations used similar low-T_g block polymers combined with rapid cross-linking after spin coating. In contrast, the much slower process used here provides enough time to lose kinetic micelle control of the micelle templates. Increasing water content, that is, increasing $\chi_{\text{core-solution}}$, from 5 to 20 wt % did not maintain kinetic micelle control with PEO-*b*-PBA. More rapid processing likely aids in limiting chain exchange; however, the results in Figure 1 demonstrate that faster processing would simultaneously thicken the skin layer and limit its extent of tailoring. In addition, changes to the skin layer thickness are expected to be convolved onto changes to the wall thickness since skin formation removes material precursors from the microparticle interiors. Thus, we adapted an alternative avenue to prevent chain exchange between micelles.

To provide more robust kinetic control, regardless of χN conditions, we used glassy-PMTs. The high-T_g core block enables micelle dynamics to be arrested thermally if good solvents and plasticizers are avoided. This strategy has been employed to halt micelle chain exchange during kinetic studies[77] for trapping diverse micelle morphologies[100−107] and was recently expanded to the context of polymer templates.[76] Glassy-PMTs were thus prepared using an established procedure based on PEO-*b*-PS. Mesoporous microparticles were again prepared with PPO using a series of M:T values and were measured by SAXS (Figure 3b). Please note that an increased water content of 10 wt % was used to maintain a narrow particle size distribution while enabling LID to limit the skin layer thickness (*vide infra*). In contrast to PEO-*b*-PBA, the SAXS trends of this sample series exhibited lattice expansion as materials were added, consistent with PMT behavior (Figures 3b and 5a) with an observed structure factor *q*-ratio of ∼1:2 in SAXS, consistent with randomly packed spheres of a relatively uniform size seen in SEM images (Figure 4).[108] These SEM images also revealed a relatively constant pore size and increasing wall thickness with M:T with the

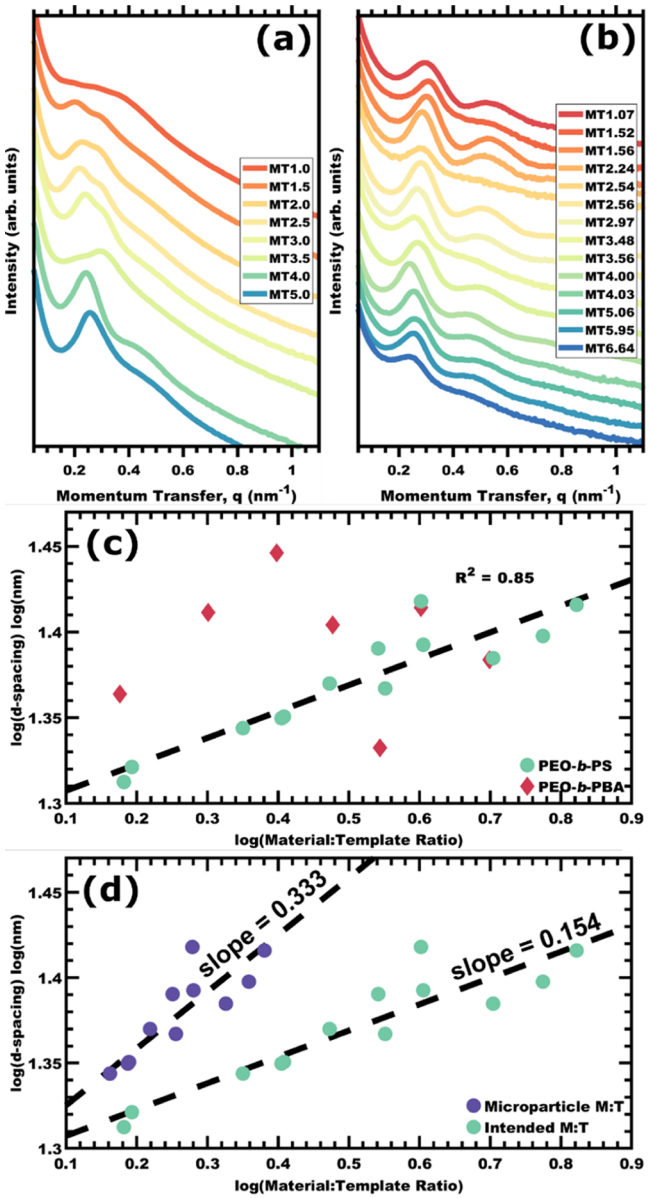

Figure 3. SAXS data for microparticle series with varied M:T values using PEO-*b*-PBA (a) were not consistent with PMT lattice expansion (c). In contrast, similar samples prepared using PEO-*b*-PS glassy-core micelles (b) show a peak shift to lower q, consistent with PMT lattice expansion (c). The PMT model predicts the log−log plots of SAXS d-spacing vs M:T to have an approximate slope of 1/3. The lower slope for the PEO-*b*-PS series was attributed to material phase separation partially into templated microparticles and partially into non-templated materials. The microparticle M:T was determined by fitting an empirical power-law relationship to correct this slope (d). Best-fit lines are presented with dashes. SAXS plots were offset vertically for clarity.

corresponding statistical descriptors presented in Figure 5. A previously developed log−log coordinate system was used to check SAXS trends for consistency with PMT conditions based upon the quantitative trend for lattice expansion (Supporting Information, eq 2).[75] In brief, an approximate slope of 1/3 is anticipated based upon the cube root relationship between volumetric attributes (M:T) and linear dimensions (d-spacing).[75] However, the PEO-*b*-PS sample series exhibited a slope of 0.154 in this log−log coordinate system (Figure 3a),

https://doi.org/10.1021/acs.langmuir.1c01865
Langmuir 2021, 37, 12874−12886

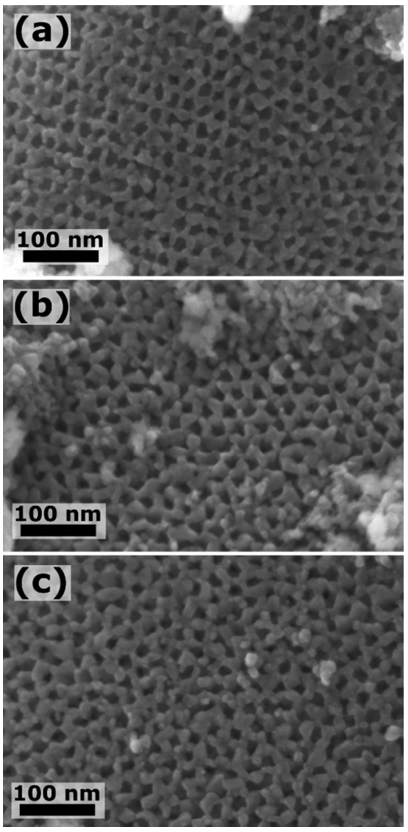

Figure 4. SEM images showing variation of wall thickness with constant pore size for the PS-*b*-PEO series: M:T = 2.54 (a), M:T = 3.48 (b), and M:T = 5.06 (c). Statistical metrics from these images and others are included in Figure 5.

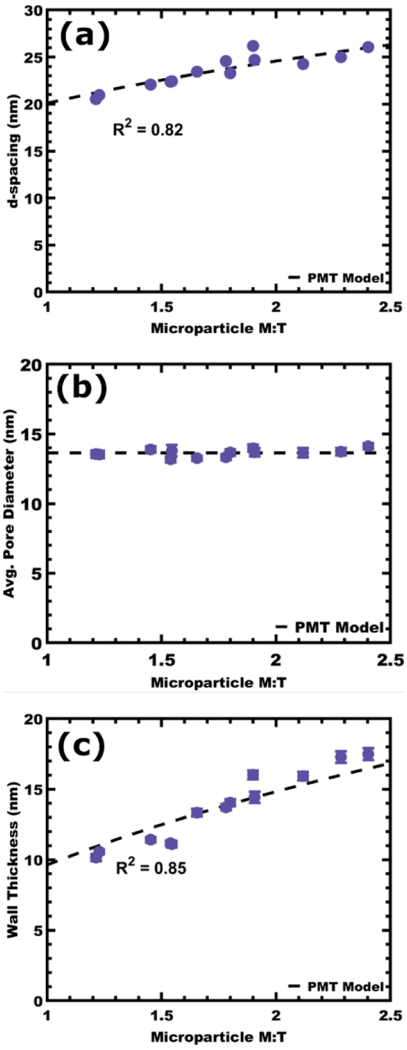

Figure 5. SAXS d-spacing with increasing microparticle M:T ratio was well-fitted by the PMT model (a). Statistical SEM measures of pore diameter (b) and wall thickness (c) were also well-fitted by the PMT model. The goodness-of-fit R^2 values are indicated.

lower than the expected value. This trend is consistent with phase separation of some material away from the micelle templates (i.e., non-templated material) (Scheme 1) or alternatively a change in material density.[75] Here, the former hypothesis is supported by SEM observations of regions of non-templated TiO_2 (Scheme 1c). The placement of material precursors away from the micelles lowers the local M:T value ("microparticle M:T") and correspondingly limits the rate of lattice expansion. A power-law relationship (Supporting Information, eq 1) was selected for convenience and simplicity to empirically resolve the discrepancy of slope by lowering the microparticle M:T value to account for material partitioning (Figure 3d). This finding suggests that all samples have some untemplated materials and that fraction increases with M:T ratio. Prior demonstrations without quantitative expectations would have easily missed such a non-templated material fraction. The increasing d-spacing trend as a function of microparticle M:T was well fitted by the PMT model[72] (Supporting Information, eqs 2−4) with a goodness-of-fit R^2 of 0.82 (Figure 5a). Consistent with PMT behavior, average SEM pore sizes were relatively constant at ∼13.6 nm for all samples measured (Figure 5b; Supporting Information, Figure S16). Furthermore, the SEM wall thickness trend (10.2−17.5 nm) was well fitted by the model with a goodness-of-fit R^2 of 0.85 (Figure 5c). Please note that the change from PEO-*b*-PBA to PEO-*b*-PS did not markedly change the TGA profile, suggesting a similar and likely negligible carbon yield (Supporting Information, Figure S15). Thus, glassy-PMT enabled the first mesoporous microparticles with independent wall thickness control from a block-polymer template with a constant mesopore size.

Briefly, it is noted that the tailored TiO_2 confinement within glassy-PMT led to systematic trends in crystallization behavior. After calcination, the resulting materials were measured using WAXS to identify the crystal structure as anatase, JCPDS Card no. 21-1272 (Figure 6a). The peak width narrowed slightly with increasing M:T, and the Scherrer formula was used to quantify the average crystallite size (Figure 6b). The average crystallite sizes exhibited an increasing trend with the M:T ratio, corresponding to larger crystallites as the wall thickness expanded as previously reported.[74] These crystallite sizes were typically about ∼80% as large as the overall wall thickness, suggesting that most crystallites had a free surface. Such crystallite size control is important for many applications in energy storage.[74,109−112] Thus, the production of mesoporous microparticles with glassy-PMT enabled tailored crystallite dimensions.

Microparticle Size Control. The microparticle size distribution determines the nominal length scale for intra-particle transport processes and thus influences performance. The microparticle size is generally expected to be determined

https://doi.org/10.1021/acs.langmuir.1c01865
Langmuir 2021, 37, 12874−12886

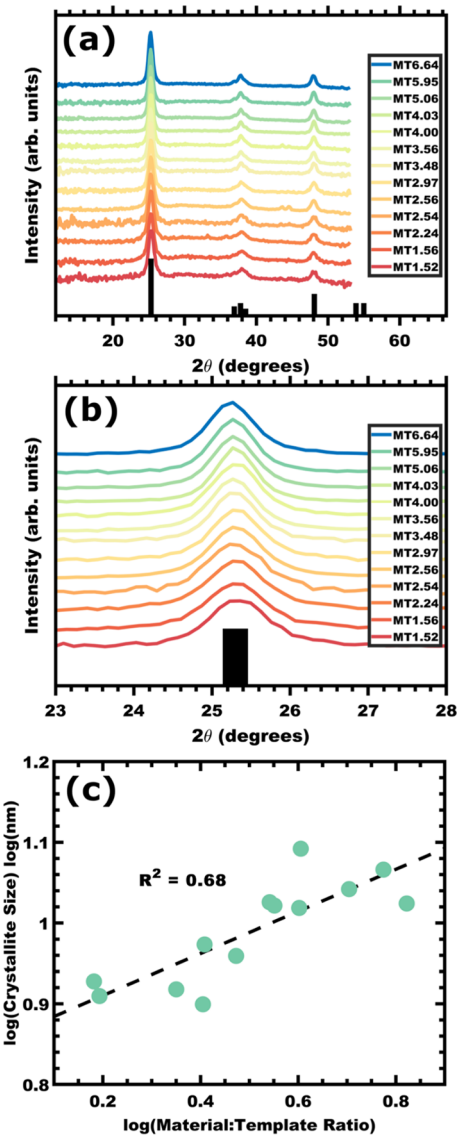

Figure 6. WAXS data for the PEO-*b*-PS sample series (a) where the (101) (b) and (200) anatase peaks were analyzed using the Scherrer formula to yield the average crystallite size (c) as a function of the M:T ratio. The reference anatase pattern is JCPDS Card no. 21-1272, and the dashed line in (c) is a guide for the eye.

kinetically by the phase separation conditions. The homopolymer is thus intended as a medium in which to disperse microparticles and avoid the formation of much larger continuous aggregates. Thus, the combination of molecular mobility and time facilitates kinetic coarsening. The initial experiments screened a range of factors from solution composition to evaporation rate, aging conditions, and the surface energy of the casting dish. The effect of homopolymer content was first investigated, with PPO mass ratios ranging from 2.0 to 40.0× with respect to the mass of the block polymer. The microparticle size distributions were determined by measurements on SEM images (Figure 7; Supporting Information, Figure S5 and Table S1). The sample with 2.5× PPO resulted in an average microparticle size of 2.36 ± 0.24 μm; however, this sample contained a significant fraction of microparticles (≥5 μm) with an uncontrolled size (Supporting Information, Figure S5a). Low amounts of PPO thus do not sufficiently separate microparticles to impede their fusion. In

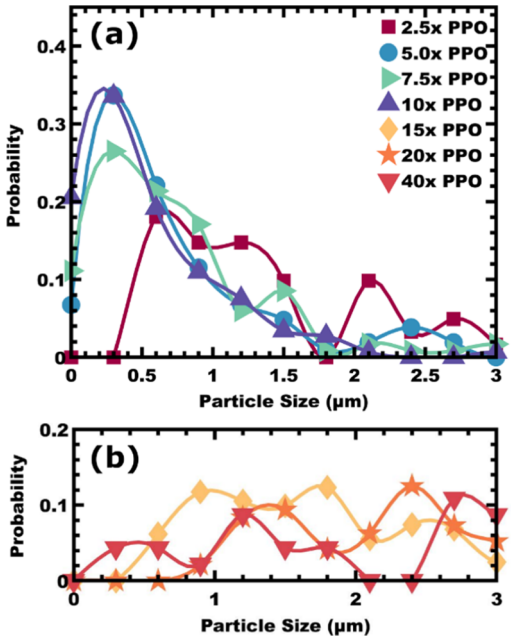

Figure 7. Microparticle size distributions were determined using measurements on SEM images as a function of different PPO ratios, where (a) contains PPO ratios from 2.5 to 10× and (b) contains ratios from 15 to 40×. The template was PEO-*b*-PBA with M:T = 2.5.

contrast, PPO ratios from 5.0 to 10.0× resulted in more uniform and smaller microparticles with average diameters of ∼1 μm (Table 1). At the other end of the continuum, PPO

Table 1. Statistical Measurements of Average Microparticle Size in Relation to Amount of PPO Added to Template Solutions Using PEO-*b*-PBA with M:T = 2.5

PPO/block polymer ratio	average particle size (μm)[a]	standard deviation (μm)
2.5	2.36 ± 0.24	1.85
5.0	1.07 ± 0.10	1.05
7.5	1.03 ± 0.08	0.91
10.0	0.72 ± 0.05	0.60
15.0	2.88 ± 0.19	2.36
20.0	4.60 ± 0.41	4.01
40.0	4.41 ± 0.47	3.20

[a]Values are reported as the average ± the error of the mean.

ratios from 15.0 to 40× exhibited an unexpected increase in microparticle size, particularly considering the dilution of the minority microparticle phase (Table 1). This accelerated coarsening was attributed to the slower solvent removal from the larger sample sizes where additional time and mobility were available for coarsening. Curiously, SEM images of microparticles with >20.0× PPO (PEO-*b*-PBA templates) were found to exhibit a morphology transition from spherical micelles to a cylindrical morphology to a worm-like morphology (Figure 8). PPO is expected to partition a fraction of water owing to its ∼1 wt % water miscibility, which lowers the water content in the microparticles, and the lowered χN barrier can enable morphology transitions.[113] This interpretation is supported by samples combining both the high water content and high PPO ratios (Supporting Information, Figure S6), where the spherical micelle morphologies were preserved. This change in morphology as

https://doi.org/10.1021/acs.langmuir.1c01865
Langmuir 2021, 37, 12874−12886

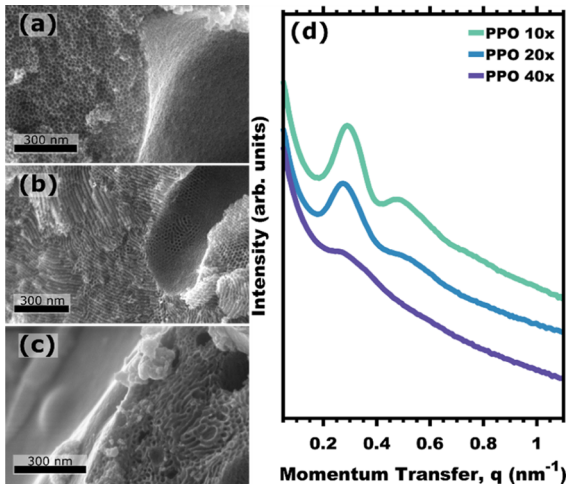

Figure 8. SEM images showing mesopore morphologies for microparticles prepared with different PPO ratios where the behavior spans from spherical pores 10× (a) to cylindrical pores 20× (b) and worm-like pores 40× (c). The corresponding SAXS patterns (d) were offset vertically for clarity. The template was PEO-*b*-PBA with M:T = 2.5.

a function of water content and PPO ratio highlights the sensitivity of non-glassy block polymer templates such as PEO-*b*-PBA and the need for glassy templates, which are less sensitive to solution conditions. Next, the effect of water content upon microparticle size was examined from 5.0 to 20 wt % water (Figure 9 and Table 2). Modest water contents

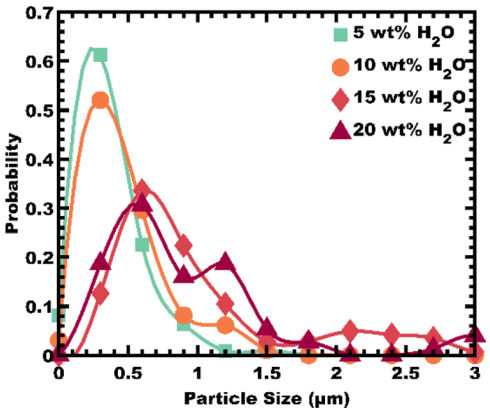

Figure 9. Microparticle size distributions as determined from SEM images were tailored as a function of the initial water quantity. The template was PEO-*b*-PBA with M:T = 2.5.

Table 2. Statistical Measurements of Average Microparticle Sizes in Relation to Water Content Using PEO-*b*-PBA Template Solutions with M:T = 2.5

water content (wt % of soln)	average particle size (μm)[a]	standard deviation (μm)
5.0	0.54 ± 0.02	0.23
10.0	0.65 ± 0.03	0.28
15.0	1.22 ± 0.06	0.77
20.0	1.18 ± 0.11	0.91

[a]Values are reported as the average ± error of the mean.

from 5.0 to 10 wt % yielded average microparticle sizes of ∼0.5 μm, whereas higher water contents from 15 to 20 wt % yielded larger average microparticles sizes of ∼1.2 μm. These samples with a higher water content were also found to exhibit a greater frequency of extended aggregates (Supporting Information, Figure S7c,d) as a higher water content enhances the mobility of the metal alkoxide oligomers,[114] increasing the hydrophobic/hydrophilic contrast and driving the phase separation. All these possible effects promote coarsening of the microparticles. The effect of substrate surface energy was also found to have a concomitant role with water content. Samples prepared in glass dishes resulted in smaller microparticles and fewer extended aggregates (Figure 9 and Table 2) when compared to Teflon dishes (Supporting Information, Figures S8 and S9 and Table S5). The attraction of the material precursors to the hydrophilic substrate could impose a drag that limits horizontal microparticle mobility and impedes coarsening. Shorter processing times prior to aging led to larger microparticles again attributed to residual solvent-induced coarsening (Supporting Information, Figure S10). Changing the molecular mass of PPO from 1 to 4 kg mol^{-1} was found to not have a significant effect on microparticle size (Supporting Information, Figures S11 and S12), suggesting that the PPO viscosity does not play a critical role in coarsening after solvent evaporation. Similarly, variation of the aging treatments was also not found to have a significant effect on microparticle size, again suggesting that the microparticle size is determined largely during evaporation (Supporting Information, Figures S13 and S14 and Table S6). While conditions with large microparticles and extended aggregates exhibited some fracturing (cleaved lines) that contribute to the particle size distribution, samples with smaller microparticles rather dominantly exhibited curved surfaces, consistent with diffusive coarsening. Please note that these PEO-*b*-PBA data on microparticle size distributions were obtained prior to the development of glassy-PMT. The presence of chain exchange, however, is not expected to significantly affect microparticle formation; thus, these parameters which tune particle size are conditions which likely do not inhibit the independent control of pore and wall feature size with glassy-PMT. Thus, numerous parameters affect the rate of microparticle coarsening during evaporative processing.

CONCLUSIONS

Mesoporous microparticles are an attractive platform for a broad set of manufacturing methods due to their convenient particulate form. The applications for TiO_2 mesoporous microparticles include catalysis, lithium-ion batteries, sensors, optoelectronics, and dye-sensitized solar cells, where each application is best matched with distinct architectural dimensions. Here, it is demonstrated for the first time that the pore size and wall thickness are independently tunable within mesoporous microparticles by using glassy-PMTs from PEO-*b*-PS. In contrast, the low-T_g PBA block in PEO-*b*-PBA was not sufficiently persistent to avoid changes to micelle size and sometimes also changes to morphology during processing. In addition, an explanation is provided for reports of surface skin layer formation which dictates transport to/from microparticle interiors. A kinetic LID model was posited where the skin layer forms due to different rates of phase separation for micelles and material precursors, followed by slow re-mixing. Here, slower evaporation enabled the thinnest skin layers and high degrees of open surface porosity which were further tunable with coarsening heat treatments. Last, the effects of several processing parameters upon the microparticle size were

https://doi.org/10.1021/acs.langmuir.1c01865
Langmuir 2021, 37, 12874−12886

examined where microparticle size was largely controlled by the removal rate of solvents.

■ ASSOCIATED CONTENT

Supporting Information

The Supporting Information is available free of charge at https://pubs.acs.org/doi/10.1021/acs.langmuir.1c01865.

NMR and GPC data of block polymers, equations for the PMT model with fit values, image of the casting dish, SAXS data of calcination series, SEM images of mesopores and microparticles, distribution plots, and TGA (PDF)

■ AUTHOR INFORMATION

Corresponding Author

Morgan Stefik − *Department of Chemistry and Biochemistry, University of South Carolina, Columbia, South Carolina 29208, United States;* orcid.org/0000-0002-2645-7442; Email: morgan@stefikgroup.com

Authors

Wessel van den Bergh − *Department of Chemistry and Biochemistry, University of South Carolina, Columbia, South Carolina 29208, United States*

Eric R. Williams − *Department of Chemistry and Biochemistry, University of South Carolina, Columbia, South Carolina 29208, United States*

Natalie Alicia Vest − *Department of Chemistry and Biochemistry, University of South Carolina, Columbia, South Carolina 29208, United States*

Pei-Hua Chiang − *Department of Chemistry and Biochemistry, University of South Carolina, Columbia, South Carolina 29208, United States*

Complete contact information is available at: https://pubs.acs.org/10.1021/acs.langmuir.1c01865

Notes

The authors declare no competing financial interest.

■ ACKNOWLEDGMENTS

W.v.d.B., E.R.W., N.A.V., P.-H.C., and M.S. would like to acknowledge support by the NSF CAREER program, NSF Award No. DMR-1752615. P.-H.C. would like to thank the UofSC SURF program for support.

■ REFERENCES

(1) Teruel, A. H.; Pérez-Esteve, É.; González-Álvarez, I.; González-Álvarez, M.; Costero, A. M.; Ferri, D.; Gaviña, P.; Merino, V.; Martínez-Máñez, R.; Sancenón, F. Double Drug Delivery Using Capped Mesoporous Silica Microparticles for the Effective Treatment of Inflammatory Bowel Disease. *Mol. Pharm.* **2019**, *16*, 2418−2429.

(2) Pavel, I.-A.; Girardon, M.; El Hajj, S.; Parant, S.; Amadei, F.; Kaufmann, S.; Tanaka, M.; Fierro, V.; Celzard, A.; Canilho, N.; Pasc, A. Lipid-coated mesoporous silica microparticles for the controlled delivery of β-galactosidase into intestines. *J. Mater. Chem. B* **2018**, *6*, 5633−5639.

(3) Qu, F.; Zhu, G.; Huang, S.; Li, S.; Sun, J.; Zhang, D.; Qiu, S. Controlled Release of Captopril by Regulating the Pore Size and Morphology of Ordered Mesoporous Silica. *Microporous Mesoporous Mater.* **2006**, *92*, 1−9.

(4) El-Boubbou, K.; Ali, R.; Al-Zahrani, H.; Trivilegio, T.; Alanazi, A. H.; Khan, A. L.; Boudjelal, M.; AlKushi, A. Preparation of Iron Oxide Mesoporous Magnetic Microparticles as Novel Multidrug Carriers for Synergistic Anticancer Therapy and Deep Tumor Penetration. *Sci. Rep.* **2019**, *9*, 9481.

(5) Arcos, D.; López-Noriega, A.; Ruiz-Hernández, E.; Terasaki, O.; Vallet-Regí, M. Ordered Mesoporous Microspheres for Bone Grafting and Drug Delivery. *Chem. Mater.* **2009**, *21*, 1000−1009.

(6) Wu, Z.; Zhao, D. Ordered Mesoporous Materials as Adsorbents. *Chem. Commun.* **2011**, *47*, 3332−3338.

(7) Qin, Z.; Zhao, Y.; Lin, L.; Zou, P.; Zhang, L.; Chen, H.; Wang, Y.; Wang, G.; Zhang, Y. Core/Shell Microcapsules Consisting of Fe_3O_4 Microparticles Coated with Nitrogen-Doped Mesoporous Carbon for Voltammetric Sensing of Hydrogen Peroxide. *Microchim. Acta* **2017**, *184*, 4513−4520.

(8) Kumar, A.; Park, G. D.; Patel, S. K. S.; Kondaveeti, S.; Otari, S.; Anwar, M. Z.; Kalia, V. C.; Singh, Y.; Kim, S. C.; Cho, B.-K.; Sohn, J.-H.; Kim, D. R.; Kang, Y. C.; Lee, J.-K. SiO_2 Microparticles with Carbon Nanotube-Derived Mesopores as an Efficient Support for Enzyme Immobilization. *Chem. Eng. J.* **2019**, *359*, 1252−1264.

(9) Zhou, X.; Zou, Y.; Ma, J.; Cheng, X.; Li, Y.; Deng, Y.; Zhao, D. Cementing Mesoporous ZnO with Silica for Controllable and Switchable Gas Sensing Selectivity. *Chem. Mater.* **2019**, *31*, 8112−8120.

(10) Chen, L.; Hu, Z.-P.; Ren, J.-T.; Wang, Z.; Yuan, Z.-Y. Efficient Oxidative Desulfurization over Highly Dispersed Molybdenum Oxides Supported on Mesoporous Titanium Phosphonates. *Microporous Mesoporous Mater.* **2021**, *315*, 110921.

(11) Sarkar, D.; Khare, D.; Kaushal, A.; Acharya, C.; Bahadur, J.; Prakash, J.; Donthula, H.; Dasgupta, K. Green and Scalable Synthesis of Nanosilver Loaded Silica Microparticles by Spray-Drying: Application as Antibacterial Agent, Catalyst and SERS Substrate. *Appl. Nanosci.* **2019**, *9*, 1925−1937.

(12) Shang, C.; Wu, Z.; Wu, W. D.; Chen, X. D. Chemical Crosslinking Assembly of ZSM-5 Nanozeolites into Uniform and Hierarchically Porous Microparticles for High-Performance Acid Catalysis. *ACS Appl. Mater. Interfaces* **2019**, *11*, 16693−16703.

(13) Khodakov, A. Y.; Griboval-Constant, A.; Bechara, R.; Zholobenko, V. L. Pore Size Effects in Fischer Tropsch Synthesis over Cobalt-Supported Mesoporous Silicas. *J. Catal.* **2002**, *206*, 230−241.

(14) Chauhan, N.; Singh, V.; Kumar, S.; Kumari, M.; Sirohi, K. Synthesis of nitrogen & palladium co-doped mesoporous titanium dioxide nanoparticles via evaporation induced self assembly method and study of their photocatalytic properties. *J. Mol. Struct.* **2019**, *1185*, 219−228.

(15) Zong, L.; Zhang, G.; Zhao, H.; Zhang, J.; Tang, Z. One Pot Synthesized CeO_2-WO_3-TiO_2 Catalysts with Enriched TiO_2 (001) Facets for Selective Catalytic Reduction of NO with NH_3 by Evaporation-Induced Self-Assembly Method. *Chem. Eng. J.* **2018**, *354*, 295−303.

(16) Zhang, W.; He, H.; Tian, Y.; Lan, K.; Liu, Q.; Wang, C.; Liu, Y.; Elzatahry, A.; Che, R.; Li, W.; Zhao, D. Synthesis of Uniform Ordered Mesoporous TiO_2 Microspheres with Controllable Phase Junctions for Efficient Solar Water Splitting. *Chem. Sci.* **2019**, *10*, 1664−1670.

(17) Zhou, W.; Li, W.; Wang, J.-Q.; Qu, Y.; Yang, Y.; Xie, Y.; Zhang, K.; Wang, L.; Fu, H.; Zhao, D. Ordered Mesoporous Black TiO_2 as Highly Efficient Hydrogen Evolution Photocatalyst. *J. Am. Chem. Soc.* **2014**, *136*, 9280−9283.

(18) Tang, C.; Liu, L.; Li, Y.; Bian, Z. Aerosol Spray Assisted Assembly of TiO_2 Mesocrystals into Hierarchical Hollow Microspheres with Enhanced Photocatalytic Performance. *Appl. Catal., B* **2017**, *201*, 41−47.

(19) Zou, M.; Xiong, F.; Ganeshraja, A. S.; Feng, X.; Wang, C.; Thomas, T.; Yang, M. Visible Light Photocatalysts (Fe, N):TiO_2 from Ammonothermally Processed, Solvothermal Self-Assembly Derived Fe-TiO_2 Mesoporous Microspheres. *Mater. Chem. Phys.* **2017**, *195*, 259−267.

(20) Liu, Z.; Wu, B.; Zhu, Y.; Yin, D.; Wang, L. Fe-Ions Modified BiOBr Mesoporous Microspheres with Excellent Photocatalytic Property. *Catal. Lett.* **2012**, *142*, 1489−1497.

(21) Cao, S.-W.; Zhu, Y.-J. Monodisperse α-Fe_2O_3 Mesoporous Microspheres: One-Step NaCl-Assisted Microwave-Solvothermal Preparation, Size Control and Photocatalytic Property. *Nanoscale Res. Lett.* **2011**, *6*, 1−7.
(22) Xu, X.; Tan, H.; Wang, Z.; Wang, C.; Pan, L.; Kaneti, Y. V.; Yang, T.; Yamauchi, Y. Extraordinary Capacitive Deionization Performance of Highly-Ordered Mesoporous Carbon Nano-Polyhedra for Brackish Water Desalination. *Environ. Sci.: Nano* **2019**, *6*, 981−989.
(23) Lu, H.; Dai, W.; Zheng, M.; Li, N.; Ji, G.; Cao, J. Electrochemical Capacitive Behaviors of Ordered Mesoporous Carbons with Controllable Pore Sizes. *J. Power Sources* **2012**, *209*, 243−250.
(24) Liu, Y.; Zhai, Y.; Xia, Y.; Li, W.; Zhao, D. Recent Progress of Porous Materials in Lithium-Metal Batteries. *Small Struct.* **2021**, *2*, 2000118.
(25) Lefrançois Perreault, L.; Colò, F.; Meligrana, G.; Kim, K.; Fiorilli, S.; Bella, F.; Nair, J. R.; Vitale-Brovarone, C.; Florek, J.; Kleitz, F.; Gerbaldi, C. Spray-Dried Mesoporous Mixed Cu-Ni Oxide@Graphene Nanocomposite Microspheres for High Power and Durable Li-Ion Battery Anodes. *Adv. Energy Mater.* **2018**, *8*, 1802438.
(26) Fischer, M. G.; Hua, X.; Wilts, B. D.; Gunkel, I.; Bennett, T. M.; Steiner, U. Mesoporous Titania Microspheres with Highly Tunable Pores as an Anode Material for Lithium Ion Batteries. *ACS Appl. Mater. Interfaces* **2017**, *9*, 22388−22397.
(27) Beitollahi, A.; Daie, A. H. H.; Samie, L.; Akbarnejad, M. M. Synthesis and Characterization of Mesoporous TiO_2 Assembled as Microspheres. *J. Alloys Compd.* **2010**, *490*, 311−317.
(28) Liu, Y.; Che, R.; Chen, G.; Fan, J.; Sun, Z.; Wu, Z.; Wang, M.; Li, B.; Wei, J.; Wei, Y.; Wang, G.; Guan, G.; Elzatahry, A. A.; Bagabas, A. A.; Al-Enizi, A. M.; Deng, Y.; Peng, H.; Zhao, D. Radially Oriented Mesoporous TiO_2 Microspheres with Single-Crystal−like Anatase Walls for High-Efficiency Optoelectronic Devices. *Sci. Adv.* **2015**, *1*, No. e1500166.
(29) Wang, Y.; Zhu, Y.; Yang, X.; Shen, J.; Li, X.; Qian, S.; Li, C. Performance Optimization in Dye-Sensitized Solar Cells with β-$NaYF_4$:Yb^{3+},Er^{3+}@SiO_2@TiO_2 Mesoporous Microspheres as Multifunctional Photoanodes. *Electrochim. Acta* **2016**, *211*, 92−100.
(30) Xiong, W.; Liu, M.; Gan, L.; Lv, Y.; Li, Y.; Yang, L.; Xu, Z.; Hao, Z.; Liu, H.; Chen, L. A Novel Synthesis of Mesoporous Carbon Microspheres for Supercapacitor Electrodes. *J. Power Sources* **2011**, *196*, 10461−10464.
(31) Liu, G.; Zhao, L.; Sun, R.; Chen, W.; Hu, M.; Liu, M.; Duan, X.; Zhang, T. Mesoporous $TiNb_2O_7$ Microspheres as High Performance Anode Materials for Lithium-Ion Batteries with High-Rate Capability and Long Cycle-Life. *Electrochim. Acta* **2018**, *259*, 20−27.
(32) Li, G.; Liu, H. Improved Electrode Performance of Mesoporous β-In_2S_3 Microspheres for Lithium Ion Batteries Using Carbon Coated Microspheres. *J. Mater. Chem.* **2011**, *21*, 18398−18402.
(33) Tu, L.; Pan, H.; Xie, H.; Yu, A.; Xu, M.; Chai, Q.; Cui, Y.; Zhou, X. Study on the Fabrication and Photovoltaic Property of TiO_2 Mesoporous Microspheres. *Solid State Sci.* **2012**, *14*, 616−621.
(34) Deng, S.; Luo, Z.; Liu, Y.; Lou, X.; Lin, C.; Yang, C.; Zhao, H.; Zheng, P.; Sun, Z.; Li, J.; Wang, N.; Wu, H. $Ti_2Nb_{10}O_{29-x}$ Mesoporous Microspheres as Promising Anode Materials for High-Performance Lithium-Ion Batteries. *J. Power Sources* **2017**, *362*, 250−257.
(35) Zhong, X.; Wang, X.; Wang, H.; Yang, Z.; Jiang, Y.; Li, J.; Tian, Z. Ultrahigh-Performance Mesoporous $ZnMn_2O_4$ Microspheres as Anode Materials for Lithium-Ion Batteries and Their in Situ Raman Investigation. *Nano Res.* **2018**, *11*, 3814−3823.
(36) Fattakhova-Rohlfing, D.; Zaleska, A.; Bein, T. Three-Dimensional Titanium Dioxide Nanomaterials. *Chem. Rev.* **2014**, *114*, 9487−9558.
(37) Juhl, A. C.; Schneider, A.; Ufer, B.; Brezesinski, T.; Janek, J.; Fröba, M. Mesoporous hollow carbon spheres for lithium-sulfur batteries: distribution of sulfur and electrochemical performance. *Beilstein J. Nanotechnol.* **2016**, *7*, 1229−1240.
(38) Wales, D. J.; Grand, J.; Ting, V. P.; Burke, R. D.; Edler, K. J.; Bowen, C. R.; Mintova, S.; Burrows, A. D.; Bowen, R.; Mintova, S.; Burrows, D. Gas sensing using porous materials for automotive applications. *Chem. Soc. Rev.* **2015**, *44*, 4290−4321.
(39) Verduzco, R.; Li, X.; Pesek, S. L.; Stein, E. G. Structure, Function, Self-Assembly, and Applications of Bottlebrush Copolymers. *Chem. Soc. Rev.* **2015**, *44*, 2405−2420.
(40) Xiao, W.; Yang, S.; Zhang, P.; Li, P.; Wu, P.; Li, M.; Chen, N.; Jie, K.; Huang, C.; Zhang, N.; Dai, S. Facile Synthesis of Highly Porous Metal Oxides by Mechanochemical Nanocasting. *Chem. Mater.* **2018**, *30*, 2924−2929.
(41) Zhang, Z.; Yang, S.; Hu, X.; Xu, H.; Peng, H.; Liu, M.; Thapaliya, B. P.; Jie, K.; Zhao, J.; Liu, J.; Chen, H.; Leng, Y.; Lu, X.; Fu, J.; Zhang, P.; Dai, S. Mechanochemical Nonhydrolytic Sol-Gel Strategy for the Production of Mesoporous Multimetallic Oxides. *Chem. Mater.* **2019**, *31*, 5529−5536.
(42) Wei, D.; Scherer, M. R. J.; Bower, C.; Andrew, P.; Ryhänen, T.; Steiner, U. A Nanostructured Electrochromic Supercapacitor. *Nano Lett.* **2012**, *12*, 1857−1862.
(43) Mei, P.; Kaneti, Y. V.; Pramanik, M.; Takei, T.; Dag, Ö.; Sugahara, Y.; Yamauchi, Y. Two-Dimensional Mesoporous Vanadium Phosphate Nanosheets through Liquid Crystal Templating Method toward Supercapacitor Application. *Nano Energy* **2018**, *52*, 336−344.
(44) Kosuge, K.; Kubo, S.; Kikukawa, N.; Takemori, M. Effect of Pore Structure in Mesoporous Silicas on VOC Dynamic Adsorption/Desorption Performance. *Langmuir* **2007**, *23*, 3095−3102.
(45) Zeleňák, V.; Badaničová, M.; Halamová, D.; Čejka, J.; Zukal, A.; Murafa, N.; Goerigk, G. Amine-Modified Ordered Mesoporous Silica: Effect of Pore Size on Carbon Dioxide Capture. *Chem. Eng. J.* **2008**, *144*, 336−342.
(46) Zhu, C.; Usiskin, R. E.; Yu, Y.; Maier, J. The Nanoscale Circuitry of Battery Electrodes. *Science* **2017**, *358*(). DOI: DOI: 10.1126/science.aao2808.
(47) Bergh, W.; Lokupitiya, H. N.; Vest, N. A.; Reid, B.; Guldin, S.; Stefik, M. Nanostructure Dependence of T-Nb_2O_5 Intercalation Pseudocapacitance Probed Using Tunable Isomorphic Architectures. *Adv. Funct. Mater.* **2021**, *31*, 2007826.
(48) Lan, K.; Wang, R.; Zhang, W.; Zhao, Z.; Elzatahry, A.; Zhang, X.; Liu, Y.; Al-Dhayan, D.; Xia, Y.; Zhao, D. Mesoporous TiO_2 Microspheres with Precisely Controlled Crystallites and Architectures. *Chem* **2018**, *4*, 2436−2450.
(49) Tong, H.; Enomoto, N.; Inada, M.; Tanaka, Y.; Hojo, J. Synthesis of Mesoporous TiO_2 Spheres and Aggregates by Sol−Gel Method for Dye-Sensitized Solar Cells. *Mater. Lett.* **2015**, *141*, 259−262.
(50) Liu, Y.; Luo, Y.; Elzatahry, A. A.; Luo, W.; Che, R.; Fan, J.; Lan, K.; Al-Enizi, A. M.; Sun, Z.; Li, B.; Liu, Z.; Shen, D.; Ling, Y.; Wang, C.; Wang, J.; Gao, W.; Yao, C.; Yuan, K.; Peng, H.; Tang, Y.; Deng, Y.; Zheng, G.; Zhou, G.; Zhao, D. Mesoporous TiO_2 Mesocrystals: Remarkable Defects-Induced Crystallite-Interface Reactivity and Their in Situ Conversion to Single Crystals. *ACS Cent. Sci.* **2015**, *1*, 400−408.
(51) Liu, Y.; Teng, W.; Chen, G.; Zhao, Z.; Zhang, W.; Kong, B.; Hozzein, W. N.; Al-Khalaf, A. A.; Deng, Y.; Zhao, D. A vesicle-aggregation-assembly approach to highly ordered mesoporous γ-alumina microspheres with shifted double-diamond networks. *Chem. Sci.* **2018**, *9*, 7705−7714.
(52) Wu, Z.; Waldron, K.; Zhang, X.; Li, Y.; Wu, L.; Wu, W. D.; Chen, X. D.; Zhao, D.; Selomulya, C. Spray-Drying Water-Based Assembly of Hierarchical and Ordered Mesoporous Silica Microparticles with Enhanced Pore Accessibility for Efficient Bio-Adsorption. *J. Colloid Interface Sci.* **2019**, *556*, 529−540.
(53) Waldron, K.; Wu, W. D.; Wu, Z.; Liu, W.; Selomulya, C.; Zhao, D.; Chen, X. D. Formation of Monodisperse Mesoporous Silica Microparticles via Spray-Drying. *J. Colloid Interface Sci.* **2014**, *418*, 225−233.
(54) Andersson, N.; Alberius, P. C. A.; Skov Pedersen, J.; Bergström, L. Structural Features and Adsorption Behaviour of Mesoporous Silica

Particles Formed from Droplets Generated in a Spraying Chamber. *Microporous Mesoporous Mater.* **2004**, *72*, 175−183.
(55) Jin, Z.; Xiao, M.; Bao, Z.; Wang, P.; Wang, J. A General Approach to Mesoporous Metal Oxide Microspheres Loaded with Noble Metal Nanoparticles. *Angew. Chem., Int. Ed.* **2012**, *51*, 6406−6410.
(56) Yu, Z.; Gao, X.; Yao, Y.; Zhang, X.; Bian, G.-Q.; Wu, W. D.; Chen, X. D.; Li, W.; Selomulya, C.; Wu, Z.; Zhao, D. Scalable Synthesis of Wrinkled Mesoporous Titania Microspheres with Uniform Large Micron Sizes for Efficient Removal of Cr(VI). *J. Mater. Chem. A* **2018**, *6*, 3954−3966.
(57) Waldron, K.; Wu, Z.; Zhao, D.; Chen, X. D.; Selomulya, C. On the Improvement of Pore Accessibility through Post-Synthesis Hydrothermal Treatments of Spray Dried SBA-15 Microspheres. *Chem. Eng. Sci.* **2015**, *127*, 276−284.
(58) Waldron, K.; Wu, Z.; Wu, W. D.; Liu, W.; Zhao, D.; Chen, X. D.; Selomulya, C. Formation of Uniform Large SBA-15 Microspheres via Spray Drying. *J. Mater. Chem. A* **2014**, *2*, 19500−19508.
(59) Wei, L.; Yan, S.; Wang, H.; Yang, H. Fabrication of Multi-Compartmentalized Mesoporous Silica Microspheres through a Pickering Droplet Strategy for Enhanced CO_2 Capture and Catalysis. *NPG Asia Mater.* **2018**, *10*, 899−911.
(60) Kuai, L.; Wang, J.; Ming, T.; Fang, C.; Sun, Z.; Geng, B.; Wang, J. Aerosol-Spray Diverse Mesoporous Metal Oxides from Metal Nitrates. *Sci. Rep.* **2015**, *5*, 9923.
(61) Baccile, N.; Grosso, D.; Sanchez, C. Aerosol Generated Mesoporous Silica Particles. *J. Mater. Chem.* **2003**, *13*, 3011−3016.
(62) Andersson, N.; Kronberg, B.; Corkery, R.; Alberius, P. Combined Emulsion and Solvent Evaporation (ESE) Synthesis Route to Well-Ordered Mesoporous Materials. *Langmuir* **2007**, *23*, 1459−1464.
(63) Oh, J. Y.; Song, S. A.; Jung, K. Y.; Chang, Y.-W.; Kim, K.; Lim, S. N.; Jeong, Y.-C. Enhancing the Light Conversion Efficiency of Dye-Sensitized Solar Cells Using Nanochannel TiO_2 Prepared by Spray Pyrolysis. *Electrochim. Acta* **2017**, *253*, 390−395.
(64) Waldron, K.; Wu, Z.; Zhao, D.; Chen, X. D.; Selomulya, C. On Spray Drying of Uniform Mesoporous Silica Microparticles. *Mater. Today* **2016**, *3*, 646−651.
(65) Tarutani, N.; Tokudome, Y.; Jobbágy, M.; Soler-Illia, G. J. A. A.; Takahashi, M. Mesoporous Microspheres of Nickel-Based Layered Hydroxides by Aerosol-Assisted Self-Assembly Using Crystalline Nano-Building Blocks. *J. Sol-Gel Sci. Technol.* **2019**, *89*, 216−224.
(66) Guan, B. Y.; Yu, L.; Lou, X. W. Formation of Asymmetric Bowl-Like Mesoporous Particles via Emulsion-Induced Interface Anisotropic Assembly. *J. Am. Chem. Soc.* **2016**, *138*, 11306−11311.
(67) Feng, Y.; Zhang, M.; Guo, M.; Wang, X. Studies on the PEG-Assisted Hydrothermal Synthesis and Growth Mechanism of ZnO Microrod and Mesoporous Microsphere Arrays on the Substrate. *Cryst. Growth Des.* **2010**, *10*, 1500−1507.
(68) Lan, K.; Liu, Y.; Zhang, W.; Liu, Y.; Elzatahry, A.; Wang, R.; Xia, Y.; Al-Dhayan, D.; Zheng, N.; Zhao, D. Uniform Ordered Two-Dimensional Mesoporous TiO_2 Nanosheets from Hydrothermal-Induced Solvent-Confined Monomicelle Assembly. *J. Am. Chem. Soc.* **2018**, *140*, 4135−4143.
(69) Zhou, H.; Xiong, H.; Zhang, R.; Zhang, L.; Zhang, L.; Li, L.; Zhang, W.; Zhu, Z.; Qiao, Z. A. A General Polymer-Oriented Acid-Mediated Self-Assembly Approach toward Crystalline Mesoporous Metal Sulfides. *Small* **2021**, *17*, 2100428.
(70) Biriaei, R.; Nohair, B.; Kaliaguine, S. A Facile Route to Synthesize Mesoporous ZSM-5 with Hexagonal Arrays Using P123 Triblock Copolymer. *Microporous Mesoporous Mater.* **2020**, *298*, 110067.
(71) Tarutani, N.; Katagiri, K.; Inumaru, K.; Ishigaki, T. Size Effect of Hydroxide Nanobuilding Blocks and Nonionic Block Copolymer Templates on the Formation of Ordered Mesoporous Structures. *J. Phys. Chem. B* **2021**, *125*, 4883−4889.
(72) Sarkar, A.; Stefik, M. How to Make Persistent Micelle Templates in 24 Hours and Know It Using X-Ray Scattering. *J. Mater. Chem. A* **2017**, *5*, 11840−11853.
(73) Lokupitiya, H. N.; Jones, A.; Reid, B.; Guldin, S.; Stefik, M. Ordered Mesoporous to Macroporous Oxides with Tunable Isomorphic Architectures: Solution Criteria for Persistent Micelle Templates. *Chem. Mater.* **2016**, *28*, 1653−1667.
(74) Lantz, K. A.; Clamp, N. B.; van den Bergh, W.; Sarkar, A.; Stefik, M. Full Gamut Wall Tunability from Persistent Micelle Templates via Ex Situ Hydrolysis. *Small* **2019**, *15*, 1900393.
(75) Sarkar, A.; Evans, L.; Stefik, M. Expanded Kinetic Control for Persistent Micelle Templates with Solvent Selection. *Langmuir* **2018**, *34*, 5738−5749.
(76) Williams, E. R.; McMahon, P. L.; Reynolds, J. E.; Snider, J. L.; Stavila, V.; Allendorf, M. D.; Stefik, M. Tailored Porous Carbons Enabled by Persistent Micelles with Glassy Cores. *Mater. Adv.* **2021**, *6*, 5381.
(77) Choi, S.-H.; Lodge, T. P.; Bates, F. S. Mechanism of Molecular Exchange in Diblock Copolymer Micelles: Hypersensitivity to Core Chain Length. *Phys. Rev. Lett.* **2010**, *104*, 047802.
(78) Ma, Y.; Lodge, T. P. Poly(Methyl Methacrylate)-*Block*-Poly(*n*-Butyl Methacrylate) Diblock Copolymer Micelles in an Ionic Liquid: Scaling of Core and Corona Size with Core Block Length. *Macromolecules* **2016**, *49*, 3639−3646.
(79) Stefik, M.; Mahajan, S.; Sai, H.; Epps, T. H.; Bates, F. S.; Gruner, S. M.; DiSalvo, F. J.; Wiesner, U. Ordered Three- and Five-Ply Nanocomposites from ABC Block Terpolymer Microphase Separation with Niobia and Aluminosilicate Sols. *Chem. Mater.* **2009**, *21*, 5466−5473.
(80) Peng, L.; Hung, C.-T.; Wang, S.; Zhang, X.; Zhu, X.; Zhao, Z.; Wang, C.; Tang, Y.; Li, W.; Zhao, D. Versatile Nanoemulsion Assembly Approach to Synthesize Functional Mesoporous Carbon Nanospheres with Tunable Pore Sizes and Architectures. *J. Am. Chem. Soc.* **2019**, *141*, 7073−7080.
(81) Park, H.; Masud, M. K.; Na, J.; Lim, H.; Phan, H.-P.; Kaneti, Y. V.; Alothman, A. A.; Salomon, C.; Nguyen, N.-T.; Hossain, M. S. A.; Yamauchi, Y. Mesoporous gold-silver alloy films towards amplification-free ultra-sensitive microRNA detection. *J. Mater. Chem. B* **2020**, *8*, 9512−9523.
(82) Iqbal, M.; Kim, Y.; Li, C.; Jiang, B.; Takei, T.; Lin, J.; Yuliarto, B.; Bando, Y.; Henzie, J.; Yamauchi, Y. Tailored Design of Mesoporous PdCu Nanospheres with Different Compositions Using Polymeric Micelles. *ACS Appl. Mater. Interfaces* **2019**, *11*, 36544−36552.
(83) Li, C.; Iqbal, M.; Jiang, B.; Wang, Z.; Kim, J.; Nanjundan, A. K.; Whitten, A. E.; Wood, K.; Yamauchi, Y. Pore-Tuning to Boost the Electrocatalytic Activity of Polymeric Micelle-Templated Mesoporous Pd Nanoparticles. *Chem. Sci.* **2019**, *10*, 4054−4061.
(84) Sarkar, A.; Thyagarajan, A.; Cole, A.; Stefik, M. Widely Tunable Persistent Micelle Templates via Homopolymer Swelling. *Soft Matter* **2019**, *15*, 5193−5203.
(85) Lokupitiya, H. N.; Stefik, M. Cavitation-enabled rapid and tunable evolution of high-χN micelles as templates for ordered mesoporous oxides. *Nanoscale* **2017**, *9*, 1393−1397.
(86) Amri, F.; Septiani, N. L. W.; Rezki, M.; Iqbal, M.; Yamauchi, Y.; Golberg, D.; Kaneti, Y. V.; Yuliarto, B. Mesoporous TiO2-Based Architectures as Promising Sensing Materials towards next-Generation Biosensing Applications. *J. Mater. Chem. B* **2021**, *9*, 1189−1207.
(87) Williams, D. B. G.; Lawton, M. Drying of Organic Solvents: Quantitative Evaluation of the Efficiency of Several Desiccants. *J. Org. Chem.* **2010**, *75*, 8351−8354.
(88) Lantz, K. A.; Sarkar, A.; Littrell, K. C.; Li, T.; Hong, K.; Stefik, M. Cavitation Enables Switchable and Rapid Block Polymer Exchange under High-χN Conditions. *Macromolecules* **2018**, *51*, 6967−6975.
(89) Docampo, P.; Guldin, S.; Steiner, U.; Snaith, H. J. Charge Transport Limitations in Self-Assembled TiO2 Photoanodes for Dye-Sensitized Solar Cells. *J. Phys. Chem. Lett.* **2013**, *4*, 698−703.
(90) Guldin, S.; Hüttner, S.; Tiwana, P.; Orilall, M. C.; Ülgüt, B.; Stefik, M.; Docampo, P.; Kolle, M.; Divitini, G.; Ducati, C.; Redfern, S. A. T.; Snaith, H. J.; Wiesner, U.; Eder, D.; Steiner, U. Improved Conductivity in Dye-Sensitised Solar Cells through Block-Copolymer Confined TiO_2 Crystallisation. *Energy Environ. Sci.* **2011**, *4*, 225−233.

(91) Docampo, P.; Guldin, S.; Stefik, M.; Tiwana, P.; Orilall, M. C.; Hüttner, S.; Sai, H.; Wiesner, U.; Steiner, U.; Snaith, H. J. Control of Solid-State Dye-Sensitized Solar Cell Performance by Block-Copolymer-Directed TiO2 Synthesis. *Adv. Funct. Mater.* **2010**, *20*, 1787−1796.
(92) Buken, O.; Mancini, K.; Sarkar, A. A Sustainable Approach to Cathode Delamination Using a Green Solvent. *RSC Adv.* **2021**, *11*, 27356−27368.
(93) Scherrer, P. Nachr Ges Wiss Goettingen. *Math. Phys.* **1918**, *2*, 98−100.
(94) Patterson, A. L. The Scherrer Formula for X-Ray Particle Size Determination. *Phys. Rev.* **1939**, *56*, 978−982.
(95) Dubinsky, S.; Park, J. I.; Gourevich, I.; Chan, C.; Deetz, M.; Kumacheva, E. Toward Controlling the Surface Morphology of Macroporous Copolymer Particles. *Macromolecules* **2009**, *42*, 1990−1994.
(96) Carroll, B.; Bocharova, V.; Carrillo, J.-M. Y.; Kisliuk, A.; Cheng, S.; Yamamoto, U.; Schweizer, K. S.; Sumpter, B. G.; Sokolov, A. P. Diffusion of Sticky Nanoparticles in a Polymer Melt: Crossover from Suppressed to Enhanced Transport. *Macromolecules* **2018**, *51*, 2268−2275.
(97) Grabowski, C. A.; Adhikary, B.; Mukhopadhyay, A. Dynamics of Gold Nanoparticles in a Polymer Melt. *Appl. Phys. Lett.* **2009**, *94*, 021903.
(98) Grabowski, C. A.; Mukhopadhyay, A. Size Effect of Nanoparticle Diffusion in a Polymer Melt. *Macromolecules* **2014**, *47*, 7238−7242.
(99) Griffin, P. J.; Bocharova, V.; Middleton, L. R.; Composto, R. J.; Clarke, N.; Schweizer, K. S.; Winey, K. I. Influence of the Bound Polymer Layer on Nanoparticle Diffusion in Polymer Melts. *ACS Macro Lett.* **2016**, *5*, 1141−1145.
(100) Zhu, J.; Hayward, R. C. Spontaneous Generation of Amphiphilic Block Copolymer Micelles with Multiple Morphologies through Interfacial Instabilities. *J. Am. Chem. Soc.* **2008**, *130*, 7496−7502.
(101) Yu, K.; Eisenberg, A. Multiple Morphologies in Aqueous Solutions of Aggregates of Polystyrene-Block-Poly(Ethylene Oxide) Diblock Copolymers. *Macromolecules* **1996**, *29*, 6359−6361.
(102) Yu, K.; Eisenberg, A. Bilayer Morphologies of Self-Assembled Crew-Cut Aggregates of Amphiphilic PS-b-PEO Diblock Copolymers in Solution. *Macromolecules* **1998**, *31*, 3509−3518.
(103) Yu, K.; Bartels, C.; Eisenberg, A. Trapping of Intermediate Structures of the Morphological Transition of Vesicles to Inverted Hexagonally Packed Rods in Dilute Solutions of PS-b-PEO. *Langmuir* **1999**, *15*, 7157−7167.
(104) Riess, G. Micellization of Block Copolymers. *Prog. Polym. Sci.* **2003**, *28*, 1107−1170.
(105) Bhargava, P.; Zheng, J. X.; Li, P.; Quirk, R. P.; Harris, F. W.; Cheng, S. Z. D. Self-Assembled Polystyrene-Block-Poly(Ethylene Oxide) Micelle Morphologies in Solution. *Macromolecules* **2006**, *39*, 4880−4888.
(106) Bhargava, P.; Tu, Y.; Zheng, J. X.; Xiong, H.; Quirk, R. P.; Cheng, S. Z. D. Temperature-Induced Reversible Morphological Changes of Polystyrene-Block-Poly(Ethylene Oxide) Micelles in Solution. *J. Am. Chem. Soc.* **2007**, *129*, 1113−1121.
(107) Mai, Y.; Eisenberg, A. Self-Assembly of Block Copolymers. *Chem. Soc. Rev.* **2012**, *41*, 5969−5985.
(108) Ruland, W.; Smarsly, B. M. Two-Dimensional Small-Angle X-Ray Scattering of Self-Assembled Nanocomposite Films with Oriented Arrays of Spheres: Determination of Lattice Type, Preferred Orientation, Deformation and Imperfection. *J. Appl. Crystallogr.* **2007**, *40*, 409−417.
(109) Wang, J.; Polleux, J.; Lim, J.; Dunn, B. Pseudocapacitive Contributions to Electrochemical Energy Storage in TiO_2 (Anatase) Nanoparticles. *J. Phys. Chem. C* **2007**, *111*, 14925−14931.
(110) Lesel, B. K.; Cook, J. B.; Yan, Y.; Lin, T. C.; Tolbert, S. H. Using Nanoscale Domain Size To Control Charge Storage Kinetics in Pseudocapacitive Nanoporous $LiMn_2O_4$ Powders. *ACS Energy Lett.* **2017**, *2*, 2293−2298.
(111) Balaya, P.; Bhattacharyya, A. J.; Jamnik, J.; Zhukovskii, Y. F.; Kotomin, E. A.; Maier, J. Nano-Ionics in the Context of Lithium Batteries. *J. Power Sources* **2006**, *159*, 171−178.
(112) Wagemaker, M.; Borghols, W. J. H.; Mulder, F. M. Large Impact of Particle Size on Insertion Reactions. A Case for Anatase LixTiO2. *J. Am. Chem. Soc.* **2007**, *129*, 4323−4327.
(113) Stefik, M.; Song, J.; Sai, H.; Guldin, S.; Boldrighini, P.; Orilall, M. C.; Steiner, U.; Gruner, S. M.; Wiesner, U. Ordered Mesoporous Titania from Highly Amphiphilic Block Copolymers: Tuned Solution Conditions Enable Highly Ordered Morphologies and Ultra-Large Mesopores. *J. Mater. Chem. A* **2015**, *3*, 11478−11492.
(114) Soler-Illia, G. J. d. A. A.; Sanchez, C. Interactions between Poly(Ethylene Oxide)-Based Surfactants and Transition Metal Alkoxides: Their Role in the Templated Construction of Mesostructured Hybrid Organic-Inorganic Composites. *New J. Chem.* **2000**, *24*, 493−499.

https://doi.org/10.1021/acs.langmuir.1c01865
Langmuir 2021, 37, 12874−12886